A Multifunctional Smart Metal Beam with Sub-Surface Embedded Sensors for Real-Time Structural Health Monitoring

SHINAN HUANG*, JINHAN REN*, PEIYUAN ZHOU,
SAZEDUR RAHMAN, KYLE YOUNG, SAZIDUR S. RAHMAN,
SANDIPAN MISHRA, JOHNSON SAMUEL,
FOTIS KOPSAFTOPOULOS and SEMIH AKIN

ABSTRACT

Smart Metallic Structures (SMS) with embedded sensors have gained significant attention for Structural Health Monitoring (SHM) applications. This study develops a "Smart Beam" with sub-surface embedded sensors, fabricated through a hybrid manufacturing approach that integrates additive and subtractive techniques. The sensor network comprises commercial off-the-shelf (COTS) sensors, including strain gauges and resistance temperature detectors (RTDs), embedded into an additively manufactured aluminum beam (Al 5356) for real-time structural health and environmental monitoring. To evaluate its performance and reliability, the fabricated beam is subjected to a series of SHM assessments, including steady-state heating, transient heating, and three-point bending experiments. The results from these tests confirm the Smart Beam's structural integrity and sensor functionality, with quantitative assessments indicating high-fidelity temperature measurements ($\leq 0.5\%$ error) and consistent strain response under both the linear and failure regions. Despite a moderate mechanical debit—20.6% reduction in flexural modulus and 18.9% in yield strength—the Smart Beam effectively captured both mechanical and thermal responses throughout testing, confirming its functional integrity and sensing reliability. The developed Smart Beam, along with its hybrid manufacturing approach, holds significant potential for advanced SHM applications.

INTRODUCTION

The integration of sensors into metallic structures has led to the emergence of "Smart Metallic Structures", which incorporate embedded sensors capable of real-time structural health monitoring (SHM) by capturing functional signals, such as strain [1], temperature [2], pressure [3], vibration [4], etc. Unlike traditional metallic structures, which require external instrumentation or periodic inspection for diagnostics [5], smart metallic structures offer continuous, real-time monitoring capabilities [6], making them well-suited for advanced SHM applications. This embedded intelligence improves reliability and facilitates predictive maintenance, particularly in mission-critical systems for early detection of potential failures.

Semih Akin, Assistant Professor, Email: akins@rpi.edu, Department of Mechanical, Aerospace and Nu- clear Engineering, Rensselaer Polytechnic Institute, Troy, NY, USA
*S.H. and J.R. contributed equally to this work.

In recent years, advances in hybrid manufacturing - which combines additive and subtractive processes - have significantly advanced the ability to embed sensors into complex geometries with high precision and structural integrity [7]. Most recently, metal AM techniques have emerged as a powerful solution for embedding sensors into intricate metallic components [8], offering both design flexibility and structural robustness for high-performance applications in demanding environments. These cutting-edge developments have opened new pathways for fabricating multifunctional metal components tailored for demanding applications where continuous SHM is critical for ensuring performance, safety, and longevity [9].

Despite significant advances in this cutting-edge domain, several critical challenges remain, including: (i) reliable sensor integration without compromising structural performance; (ii) seamless sensor-packaging with strong and robust interfaces between dissimilar (heterogeneous) materials; (iii) long-term durability under operational conditions; and (iv) scalable manufacturing of smart metals for large-scale applications. Addressing these challenges is essential for the widespread deployment of smart metallic structures across various fields and will depend heavily on the advancement of innovative, non-conventional manufacturing approaches.

Therefore, the main objective of this work is to develop and demonstrate a "Smart Beam" with sub-surface embedded sensors using an innovative hybrid manufacturing approach. To this end, the beam is designed to incorporate commercial off-the-shelf (COTS) sensors, including strain gauges and temperature sensors. The sensors are then embedded beneath the surface (i.e., sub-surface) of the host metal structure, which is fabricated via wire arc additive manufacturing (WAAM) followed by subtractive machining. Subsequently, a protective ceramic layer is deposited over the embedded sensors to safeguard them during subsequent metal AM processes. Lastly, the fabricated Smart Beam is subjected to a series of SHM tests, including thermal evaluations under steady-state and transient conditions, and mechanical testing via three-point bending, to assess sensor performance, signal stability, and structural integrity. Taken together, this work presents a novel framework for fabricating smart metallic structures with sub-surface integrated sensing capabilities for advanced SHM applications.

FABRICATION OF SMART METAL BEAM

A smart beam is designed with subsurface-embedded sensors by employing COTS sensors. As shown in Fig. 1a, the beam incorporates two strain gauges (SG, *OMEGA, SGT-2/350-XY43*) and three resistance temperature detectors (RTDs, *OMEGA, F3105*), all embedded into the subsurface of the beam. Representative images of the COTS sensors used in this work are presented in Fig. 1b. The fabrication of the smart beam, which features sub-surface embedded SGs and RTDs, involves the following steps (see Fig. 1c):

Step 1) Wire arc additive manufacturing (WAAM) to build the host structure

Step 2) Subtractive machining of the sensor cavities, followed by sensors attachment

Step 3) Deposition of a ceramic layer to protect the sensors from environmental exposure (e.g., moisture, temperature, corrosion, mechanical abrasion).

Step 4) Surface metallization over the ceramic layer to fully package the sensors.

Step 5) Wiring the embedded sensors to enable full functionality of the "Smart Beam," as presented in Fig. 1d.

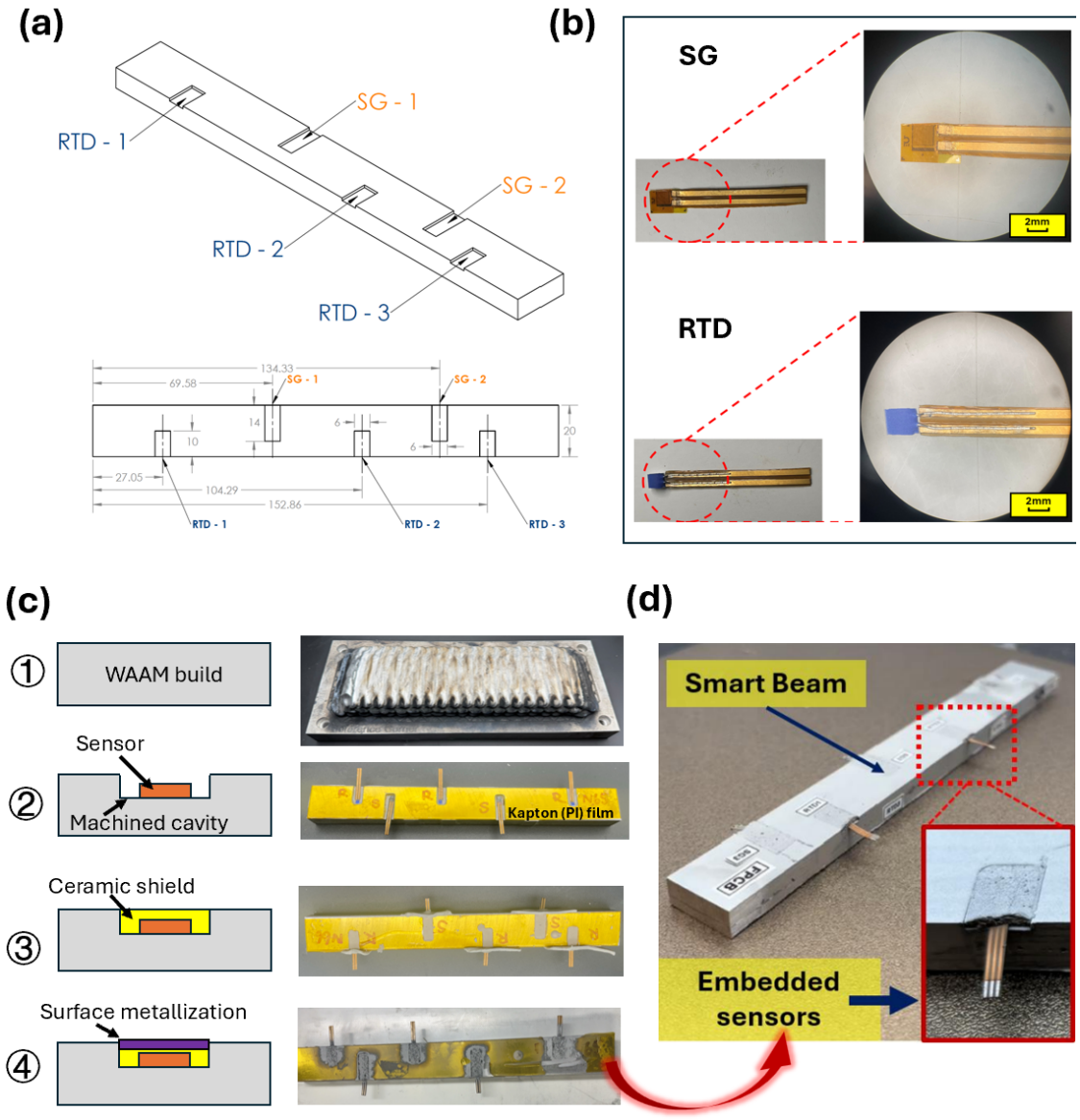

Figure 1. (a) Design of the "Smart Metal Beam" with subsurface embedded sensors: Isometric view (top panel) and front view with corresponding dimensions (bottom panel); (b) Representative images of the COTS strain (upper panel) and temperature sensors (bottom panel); (c) Fabrication steps of the Smart Beam; (d) Fabricated Smart Beam.

Smart beam fabrication begins with building the host metal structure via WAAM, using 5356 Al-Mg alloy as the feedstock wire. The process is controlled by multi-axis robotic arms (*Yaskawa*) within a sensor-rich WAAM cell, as described in Ref [10]. The host metal structure was fabricated using the WAAM process parameters listed in Table 1, which enabled effective control of the molten pool during material deposition.

After constructing the host metal structure, sensor cavities were machined subtractively using a computer numerical control (CNC) mill (*HAAS CNC Mill)*. Three cavities (10 mm × 6 mm × 2 mm) were created on the top surface for embedding RTD sensors, and two cavities (14 mm × 6 mm × 2 mm) were machined for SGs (Fig. 1a, bottom

panel). Next, the sensors were integrated into the flexible printed circuit board (FPCB) packaging via off-line spot welding (see Fig. 1c, Step 2). The packaged sensors were subsequently bonded into the machined cavities using a dedicated bonding agent (*M-Bond 610*), in accordance with the standard sensor installation procedure [11].

After sensor bonding, a layer of ceramic paste was applied over the sensors, ensuring contact with the underlying metal substrate. This layer acts as a protective barrier, shielding the sensors from environmental stressors such as high temperatures, oxidation, moisture, and mechanical abrasion (see Fig. 1c, Step 3). The ceramic paste was then cured for 24 hours at room temperature, remaining in a green (semi-sintered) state and retaining a degree of ductility. This ductility is critical for the subsequent cold spray metallization process, as it enables the ceramic layer to absorb the impact of high-velocity particles without incurring damage. During the subsequent WAAM stage, the ceramic layer undergoes further sintering as a result of heat transfer from the wire arc process. Overall, the semi-cured ceramic offers the necessary compliance to facilitate effective cold spray deposition, while completing its curing during the WAAM process.

Subsequently, the surface of the ceramic layer was metallized using the Cold Spray Additive Manufacturing (CSAM) technique, which is an emerging solid-state deposition process known for its low-temperature operation and ability to produce dense metallic coatings [12]. In this regard, an aluminum-rich powder mixture was deposited onto the ceramic layer using the CSAM process settings provided in Table 1, ensuring seamless integration with the host metal structure for robust sensor protection (see Fig. 1d).

Following CSAM-based metallization, the sensor wires were connected to a data acquisition (DAQ) unit (*NI, DAQexpress*) using a conventional tin-lead soldering process to enable real-time SHM during a series of tests described in the subsequent sections.

Table 1. Fabrication parameters for the developed hybrid manufacturing approach.

Fabrication Process	**Parameter**	**Value (unit)**
Step-1 WAAM	Material	Aluminum (Al-5356)
	Wire feed rate	400 inch/min ($\sim$ 0.17 m/s)
	Torch speed	4 mm/sec
	Number of weld beads	20
	Beads (hatch) distance	6 mm
Step-2 Machining	Cutting tool	3.175 mm ball end mill
	Spindle speed	4,000 rpm
	Feed rate	2 inch/min ($\sim$ 50.8 mm/min)
Step-3 Surface metallization	Material	Mixture of Al, Al_2O_3, and Zn
	Gas temperature	400 °C
	Gas pressure	6 bar (0.6 MPa)
	Nozzle transverse speed	20 mm/sec
	Nozzle stand-off distance	25 mm

STRUCTURAL HEALTH MONITORING

In this section, the fabricated Smart Beam is subjected to a series of SHM assessments, including: (i) steady-state heating; (ii) transient heating; and (iii) three-point bending tests. These evaluations are designed to assess the beam's ability to accurately sense and respond to thermal and mechanical stimuli in real-time across a range of operating conditions. Detailed descriptions of each test are provided below.

Steady-state thermal analysis

According to the IEC-60751 standard [13], the relationship between resistance and temperature for RTDs is described by the following expression:

$$R(T) = R_0(1 + AT + BT^2), \tag{1}$$

where $R(T)$ denotes the electrical resistance at temperature T (in $^\circ$C), and R_0 is the nominal resistance at $0\,^\circ\mathrm{C}$. The coefficients A and B capture the temperature-dependent behavior of the RTD, with standard values given by $A = 3.908 \times 10^{-3}\,^\circ\mathrm{C}^{-1}$ and $B = -5.775 \times 10^{-7}\,^\circ\mathrm{C}^{-2}$, respectively.

However, due to variations introduced during the manufacturing process and manual soldering of the sensing elements, the actual characteristics of each RTD may deviate from the nominal specifications. As a result, the standard parameters R_0, A, and B may no longer accurately represent the resistance-temperature behavior of a given sensor. To account for these discrepancies, calibration experiments were conducted in a controlled thermal environment (see Fig. 2a, left panel), enabling the accurate determination of a customized resistance-temperature relationship for each individual RTD.

During the calibration experiment, four thermocouples (TCs) were attached to the surface of the beam to serve as ground-truth temperature references (see Fig. 2a, right panel). The temperature recorded by the TCs reflect the actual temperature of the thermal chamber. Data were collected under steady-state conditions at eight target temperatures, ranging from $50\,^\circ\mathrm{C}$ to $120\,^\circ\mathrm{C}$, with an increment of $10\,^\circ\mathrm{C}$.

The average temperature of the four TCs was used as a reference for each data point. Since the maximum temperature in the experiment was $120\,^\circ\mathrm{C}$, and the quadratic coefficient B in the standard resistance-temperature model is inherently small, the quadratic term was considered negligible. Therefore, a linear approximation was considered sufficient to model the resistance-temperature relationship of each RTD:

$$R(T) \approx \alpha T + \beta, \tag{2}$$

where α and β are calibration-specific parameters obtained by fitting the least squares.

Two of the eight collected datasets (50°C and 110°C) were randomly selected as a training set to determine the parameters, while the remaining six were used to validate the fitted model. Table 2 summarizes the relative errors between the calibrated RTD readings and the reference TC temperatures, providing a quantitative assessment of calibration accuracy. The resulting linear models showed high accuracy, with the relative fitting error within 0.5%, as shown in Fig. 2b. As such, the results confirmed that

the RTDs embedded within the subsurface of the beam can effectively sense surrounding temperatures, thereby highlighting the potential of subsurface-embedded RTDs as viable sensing elements for internal thermal characterization, structural diagnosis, and environmental monitoring. Moreover, the integration of RTDs within the beam can enable real-time thermal feedback on critical factors such as thermal gradients, localized heating, and potential thermal failures.

Table 2. Relative error for embedded RTDs under calibration conditions.

Temperature (°C)	RTD 1 Error	RTD 2 Error	RTD 3 Error
50	0.0972%	0.114%	0.0993%
60	0.263%	0.370%	0.360%
70	0.267%	0.336%	0.363%
80	0.257%	0.293%	0.324%
90	0.170%	0.178%	0.204%
100	0.0629%	0.0582%	0.0755%
110	0.0571%	0.0673%	0.0584%
120	0.174%	0.190%	0.190%

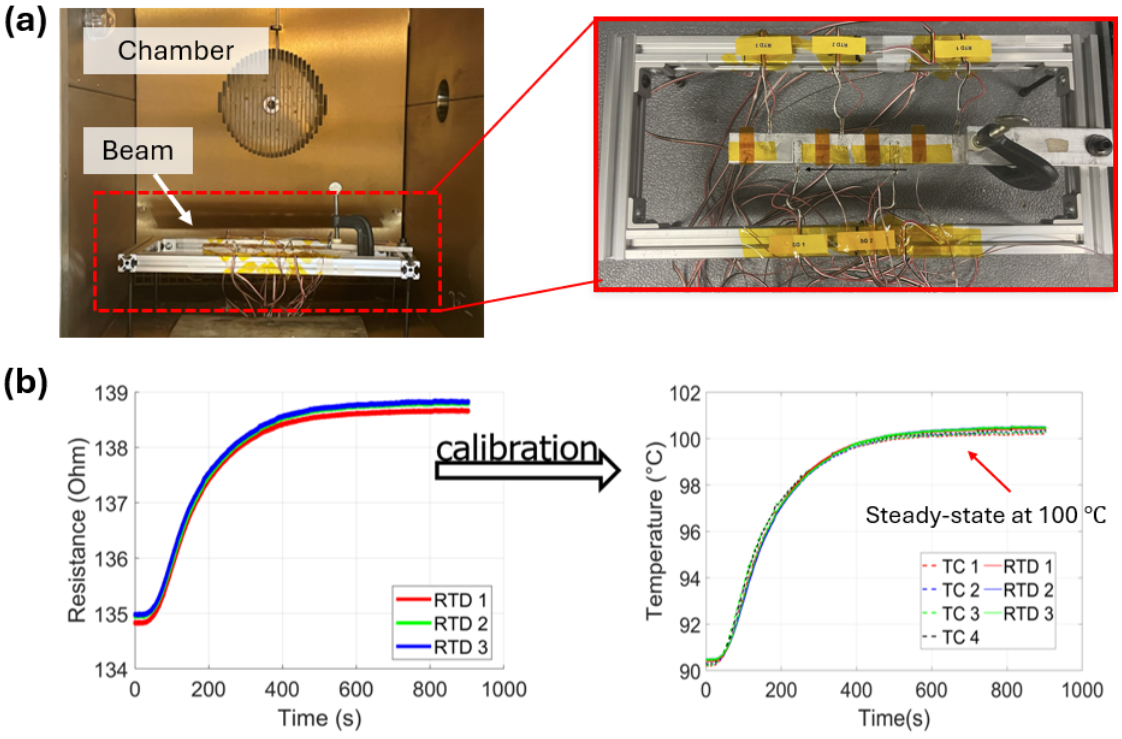

Figure 2. Steady-state thermal SHM experiments: (a) Experimental setup used for RTD sensor calibration and thermal experiments; (b) Calibration of the RTDs at 100 °C.

Transient thermal analysis

Although steady-state results establish the sensing reliability of embedded RTDs, it is also essential to examine their behavior under dynamically varying (transient) thermal conditions. To investigate the transient thermal characteristics of embedded RTDs, a controlled thermal excitation was applied using a programmable heater (*F4T temperature controller*) mounted on the leftmost surface of the beam (see Fig. 3a). The heater was driven according to a predefined thermal loading sequence involving a transient temperature input, simulating transient thermal events. Thermocouples (TC 1-TC 4) and RTDs (RTD 1-RTD 3) were used for cross-validation, with TC 1 was placed directly below the heater to measure the actual thermal input (see Fig. 3b).

Fig. 3c compares the temperature measured by RTD 1 with the real-time surface temperature at the heater location, as measured by TC 1. Due to the presence of feedback control in the heating system, the temperature input does not follow a smooth transient profile, but instead exhibits a stepwise increase. As such, RTD 1 captured a delayed and smoother temperature response as a result of thermal conduction through the beam material. Nevertheless, the sub-surface measurement of RTD 1 successfully tracks the overall surface temperature trend, demonstrating its ability to sense dynamic thermal input with high fidelity. At locations farther away from the heat source, including TC 2–TC 4 and RTD 2–RTD 3, the temperature variations are less pronounced due to the influence of convective heat loss (see Fig. 3d). These sensors exhibit closely aligned trends in their temperature evolution, indicating consistent thermal propagation throughout the beam. The embedded RTDs in these regions effectively captured dynamic temperature changes, further underscoring their ability to sense temporally varying thermal fields even under reduced thermal gradients.

Mechanical tests

The three-point bending experiments were conducted for two main purposes: (i) to verify the functionality of the SGs and (ii) to compare the mechanical properties of the beam with subsurface-embedded sensors against those of baseline beams (i.e., beams without sensors). To verify the functionality of the embedded SGs, tests were performed within the elastic deformation region, focusing on the linear response range. A displacement-controlled loading profile was applied at a constant rate of 1.067 mm/min until the actuator reached a displacement of 0.5 mm, followed by a 2-minute hold for stabilization. Two surface-mounted SGs (SG 1 and SG 2) on the beam's tensile side served as references: SG 1 was placed at mid-span (60 mm from each support), and SG 2 was positioned 10 mm from the nearest support (see Fig. 4a).

Fig. 4b shows the measured strain responses from all SGs. All gauges accurately tracked the applied load variations, confirming their proper functionality. The subsurface SGs recorded compressive strain (negative values) consistent with their location on the compression side of the neutral axis, while the surface-mounted reference SGs recorded tensile strain (positive values). Additionally, as expected from the bending stress distribution, SGs positioned closer to the beam's center experienced larger strain magnitudes, further confirming the accuracy and reliability of the embedded SGs in capturing localized mechanical responses under flexural loading.

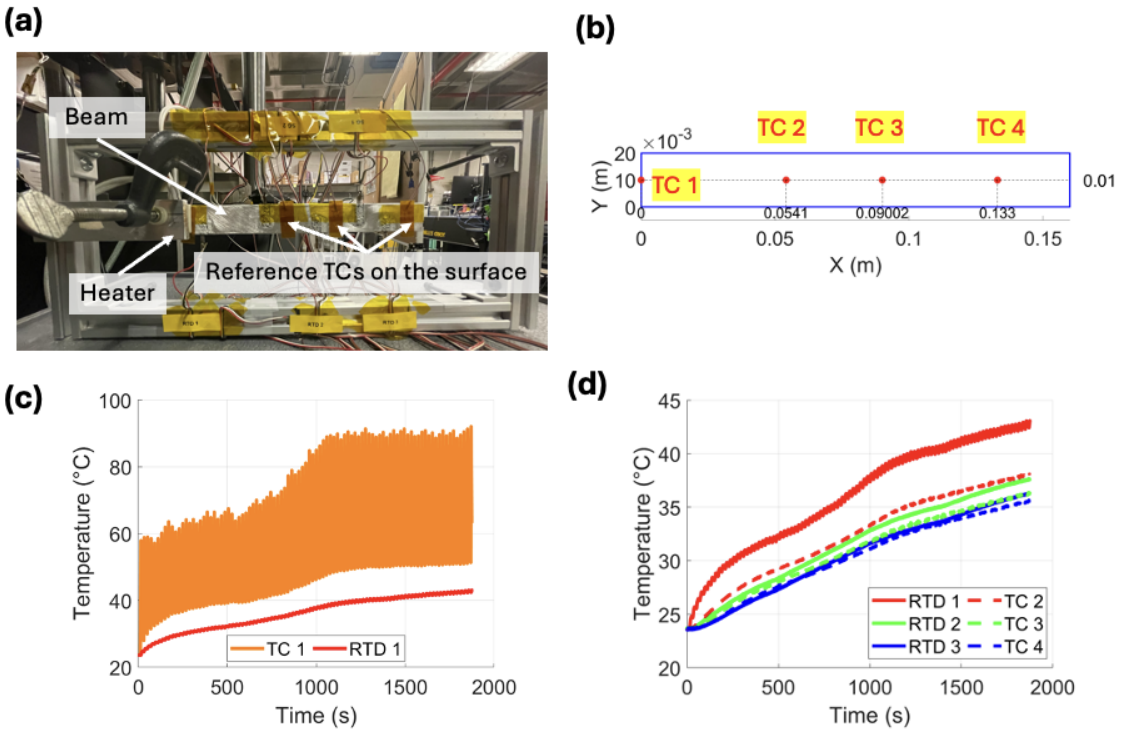

Figure 3. Transient thermal SHM experiments: (a) Experimental setup for the transient thermal response test; (b) Locations of the reference TCs on the beam surface; (c) Comparison between TC 1 and RTD 1 measurements (*Note: TC1 is near the ceramic heater*); (d) Response of the embedded RTDs and reference TCs under transient thermal input.

Following the validation of the embedded strain gauges, a mechanical test was performed to evaluate the beam's structural properties. The beam was loaded under displacement control at 1.846mm/min until yielding and eventual failure. As shown in Fig. 4c, the test captured the load response and flexural strain behavior, enabling the extraction of key properties such as flexural modulus, yield strength, failure strain, and maximum flexural stress. These metrics provide a quantitative basis for assessing the effect of subsurface-embedded sensors.

As shown in Table 3, subsurface sensors led to a moderate reduction in both stiffness and strength. The flexural modulus of the Smart Beam dropped by 20.6%, indicating reduced bending stiffness, while yield strength decreased by 18.9%, reflecting diminished resistance to plastic deformation. However, failure strain declined by only 3.6%, suggesting that ductility was largely preserved despite sensor integration.

Table 3. Comparative summary of mechanical performance under three-point bending for the Smart Beam and the baseline beam.

Property	**Baseline beam**	**Smart Beam**	**Mechanical Debit (%)**
Flexural Modulus E_{SG} (GPa)	66.12	52.49	20.6
Yield Strength (MPa)	148.24	120.4	18.9
Failure Strain	0.0773	0.075	3.6

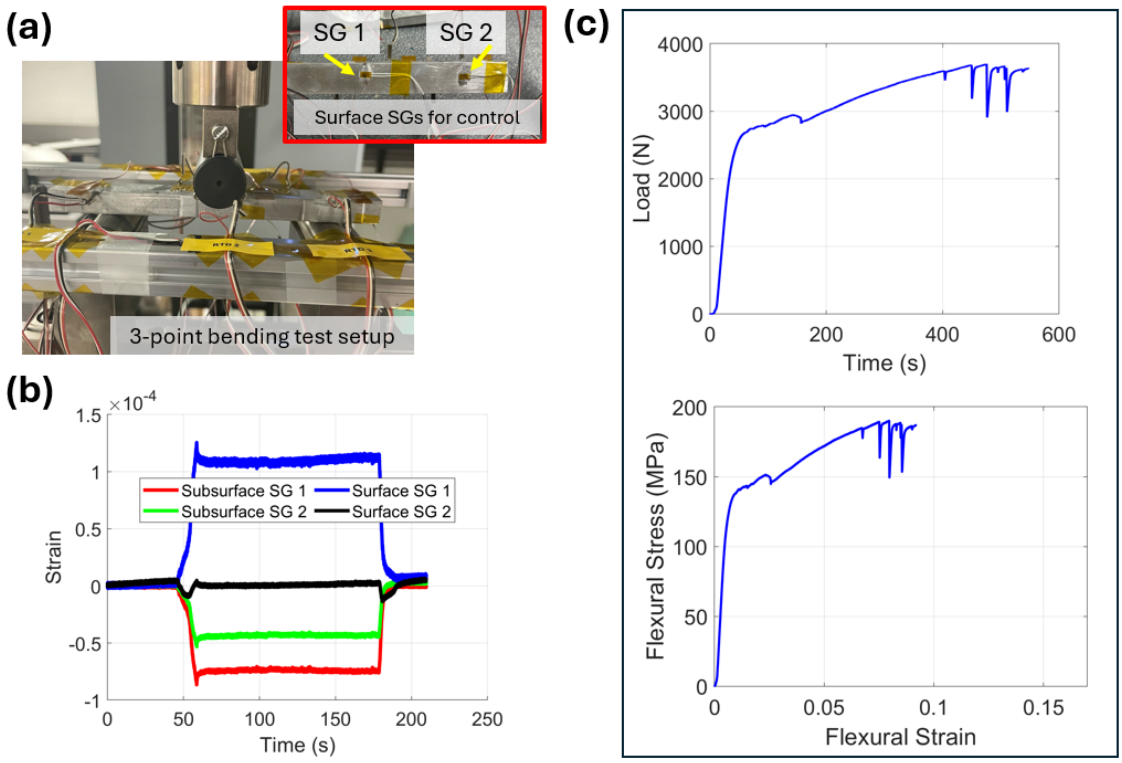

Figure 4. Mechanical SHM experiments: (a) Experimental setup for the mechanical (3-point bending) characterization; (b) Linear range strain evaluation over time; (c) Load variation over time (top panel) and flexural strain versus flexural stress (bottom panel).

DISCUSSION

The SHM assessments, encompassing both steady-state and transient heating as well as three-point bending tests, confirmed the effectiveness of the developed Smart Beam for real-time SHM. Particularly, embedded RTDs demonstrated high accuracy in sensing temperature variations, effectively capturing both steady-state and transient thermal responses. Furthermore, embedded SGs accurately tracked variations in the applied load, confirming their reliable functionality. These promising results collectively demonstrated the capabilities of the Smart Beam achieved through an innovative hybrid manufacturing approach.

Notably, the proposed hybrid manufacturing approach (see Fig. 1) holds strong potential for fabricating functional interlayers that could be compatible with various AM processes (e.g., WAAM, laser-directed energy deposition, laser powder bed fusion). This feature can facilitate the seamless resumption of the AM processes on the sensor-integrated beam. It is particularly important, as many AM techniques face challenges in achieving strong and conformal interlayers to ensure reliable bonding and structural continuity during process resumption. As such, the proposed hybrid manufacturing pathway can effectively address the relevant limitations of conventional approaches.

Despite these promising results, the Smart Beam exhibited a moderate reduction in both stiffness and strength compared to the baseline beams. This mechanical debit is likely attributed to the presence of the machined sensor cavities, which act as stress con-

centrators within the structure. However, it should be noted that the mechanical debit data was obtained from a single specimen (i.e., single data point) and therefore requires further investigation through repeating testing and statistical analysis to ensure reproducibility and reliability. To enhance the mechanical debit, the following strategies may be considered: (i) optimizing sensor network; (ii) leveraging simulation-assisted temperature and strain field estimation using a reduced number of sensors; and (iii) refining the manufacturing process to alleviate stress concentrators within the host structure.

CONCLUDING REMARKS

In this study, we presented a multifunctional Smart Metal Beam with subsurface-embedded sensors, fabricated through an innovative hybrid manufacturing approach. WAAM was used to build the host structure, followed by subtractive machining of the sensor cavities to embed SG and RTD sensors. A ceramic layer coating was applied over the sensors to securely pack them into cavities while also providing structural reinforcement for the subsequent AM process. Lastly, cold spray was employed to deposit a thin layer of seamless metal film onto the ceramic to achieve fully encapsulated embedded sensors. The following conclusions can be drawn from the present study:

- The temperature signals from the embedded sensors were successfully calibrated against external sensors, with an error margin of 0.5% for RTDs.
- The calibrated temperature sensors (RTDs) exhibited consistent and high-fidelity temperature responses under both steady-state and transient conditions.
- Subsurface SGs exhibited consistent and high-fidelity strain response under both linear range and load-to-fail conditions throughout three-point bending experiments. This confirmed the reliability of embedded SGs for SHM across a wide range of mechanical stresses.
- The developed Smart Beam demonstrated a moderate mechanical debit, with reductions of 20.6%, 18.9%, and 3.6% in flexural modulus, yield strength, and failure strain, respectively, compared to the baseline beam. Despite this trade-off, the beam holds promising structural performance for embedded sensing applications.

In summary, this study validated the developed Smart Beam and its hybrid manufacturing approach as a promising framework for advanced SHM applications. These efforts can open new aveneus for designing and development of intelligent, multifunctional metal structures. Future work will focus on expanding the sensing modalities and assessing the long-term durability of the Smart Beams under dynamic and cyclic loading conditions to support field-ready implementation.

ACKNOWLEDGMENT

This work was performed under agreement (# HR00112490367) between the Defense Advanced Research Projects Agency (DARPA) and Rensselaer Polytechnic Institute (RPI). Internal funding from RPI is also acknowledged.

REFERENCES

1. Hyer, H. C., D. C. Sweeney, and C. M. Petrie. 2024. "Distributed strain sensing using Bimetallic coated fiber optic sensors embedded in stainless steel," *Additive Manufacturing*, 91:104355, doi:10.1016/j.addma.2024.104355.
2. Bian, Q., A. Podhrazsky, C. Bauer, A. Stadler, F. Buchfellner, R. Kuttler, M. Jakobi, W. Volk, A. W. Koch, and J. Roths. 2022. "Temperature and external strain sensing with metal-embedded optical fiber sensors for structural health monitoring," *Optics Express*, 30(19):33449–33464, doi:10.1364/OE.459459.
3. Kim, C., H. Oh, B. C. Jung, and S. J. Moon. 2022. "Optimal sensor placement to detect ruptures in pipeline systems subject to uncertainty using an Adam-mutated genetic algorithm," *Structural Health Monitoring*, 21(5):2354–2369, doi:10.1177/14759217211056557.
4. Khattak, M. M., L. M. Headings, and M. J. Dapino. 2023. "Dynamic Response of a Polyvinylidene Fluoride (PVDF) Sensor Embedded in a Metal Structure Using Ultrasonic Additive Manufacturing," *Actuators*, 12(11):428, doi:10.3390/act12110428.
5. Lu, C.-L., H. He, J. Ren, J. Dhar, G. Saunders, A. Julius, J. Samuel, and J. T. Wen. 2025. "Multi-Robot Scan-n-Print for Wire Arc Additive Manufacturing," *ASME Letters in Translational Robotics*, 1(1):011003.
6. Mardanshahi, A., A. Sreekumar, X. Yang, S. K. Barman, and D. Chronopoulos. 2025. "Sensing Techniques for Structural Health Monitoring: A State-of-the-Art Review on Performance Criteria and New-Generation Technologies," *Sensors*, 25(5):1424, doi:10.3390/s25051424.
7. Hyer, H. C., D. C. Sweeney, and C. M. Petrie. 2022. "Functional fiber-optic sensors embedded in stainless steel components using ultrasonic additive manufacturing for distributed temperature and strain measurements," *Additive Manufacturing*, 52:102681, ISSN 2214-8604, doi:https://doi.org/10.1016/j.addma.2022.102681.
8. Jung, I. D., M. S. Lee, J. Lee, H. Sung, J. Choe, H. J. Son, J. Yun, K. bong Kim, M. Kim, S. W. Lee, S. Yang, S. K. Moon, K. T. Kim, and J.-H. Yu. 2020. "Embedding sensors using selective laser melting for self-cognitive metal parts," *Additive Manufacturing*, 33:101151, ISSN 2214-8604, doi:https://doi.org/10.1016/j.addma.2020.101151.
9. Ferreira, P. M., M. A. Machado, M. S. Carvalho, and C. Vidal. 2022. "Embedded Sensors for Structural Health Monitoring: Methodologies and Applications Review," *Sensors*, 22(21):8320, doi:10.3390/s22218320.
10. He, H., C.-l. Lu, J. Ren, J. Dhar, G. Saunders, J. Wason, J. Samuel, A. Julius, and J. T. Wen. 2025. "Open-source software architecture for multi-robot Wire Arc Additive Manufacturing (WAAM)," *Applications in Engineering Science*, 22:100204.
11. Vishay Precision Group. 2015, "Instruction Bulletin B-130-15: Strain Gage Installation with M-Bond 610 Adhesive," https://intertechnology.com/Vishay/pdfs/Instruction_Bulletins/B-130-15.pdf.
12. Akin, S., S. Lee, S. Jo, D. G. Ruzgar, K. Subramaniam, J.-T. Tsai, and M. B.-G. Jun. 2022. "Cold spray-based rapid and scalable production of printed flexible electronics," *Additive Manufacturing*, 60:103244.
13. Ricci, S. 2024. "Multichannel Emulator for Resistance Temperature Detectors (RTDs)," *IEEE Transactions on Industrial Electronics*.